Astronomy and Computing 14 (2016) 43–51

Contents lists available at ScienceDirect

Astronomy and Computing

journal homepage: www.elsevier.com/locate/ascom

Full length article

Dynamic process analysis by moments of extreme orders

S. Šimberová [a,*], T. Suk [b]

[a] Astronomical Institute, The Czech Academy of Sciences, 251 65 Ondřejov, Czech Republic
[b] Institute of Information Theory and Automation, The Czech Academy of Sciences, 182 08 Prague 8, Czech Republic

ARTICLE INFO

Article history:
Received 3 December 2014
Accepted 9 January 2016
Available online 18 January 2016

Keywords:
High-order moments
Principal component analysis
Frequency analysis
Solar flares

ABSTRACT

Dynamic processes in astronomical observations are captured in various video sequences. The image datacubes are represented by the datasets of random variables. Diagnostics of a fast developing event is based on the specific behavior of the high-order moments (HOM) in time. The moment curves computed in an image video sequence give valuable information about various phases of the phenomenon and significant periods in the frequency analysis. The proposed method uses statistical moments of high and very high orders to describe and investigate the dynamic process in progress. Since these moments are highly correlated, the method of principal component analysis (PCA) has been suggested for following frequency analysis. PCA can be used both for decorrelation of the moments and for determination of the number of used moments. We experimentally illustrate performance of the method on simulated data. A typical development of the dynamic phenomenon is modeled by the moment time curve. Then applications to the real data sequences follow: solar active regions observed in the spectral line Hα (wavelength 6563 Å—Ondřejov and Kanzelhöhe observatories) in two different angular resolutions. The frequency analysis of the first few principal components showed common periods or quasi-periods of all examined events and the periods specific for individual events. The detailed analysis of the moment's methodology can contribute to the observational mode settings. The method can be applied to video sequences obtained by observing systems with various angular resolutions. It is robust to noise and it can work with high range of sampling frequencies.

1. Introduction

Many natural-science branches solve a common problem with the processing of a video sequence to get valuable information about the records. The ground-based and satellite astronomical observations incorporate video sequences showing various types of events: from stable scene up to the highly dynamic process. The current methods of processing strongly depend not only on the kind of data but also on the ongoing events in video sequences. The image data (2D, 3D, etc.) are represented by the datasets of random variables and from these modeled and/or observed datacubes information is obtained about the events in progress. The dynamic process in astronomy can appear in different kinds of observations, e.g. records of meteoric swarms, flashes of gamma lighting [in seconds], solar flares and prominences [in minutes], etc.

To perform a valuable diagnostics of an event we have chosen statistical moments. Moments are widely used in statistical analysis. Generally they give information about the distribution of data on various platforms. For practical use of moments in statistics, see e.g. Dudewicz and Mishra (1988).

If we choose the moment as a characteristic, then we still have a few options; we can consider the image itself to be a realization of a random field and compute two-dimensional moments from them. This approach is often used in the field of signal processing, image analysis and pattern recognition, see Flusser et al. (2009). Another option is to consider the image histogram as an estimate of a probability density function. In this paper we have chosen the latter one; we are interested in signal evolution in time and this option enables a suitable way how to suppress the spatial information. We still need to select the optimal order of the moments.

Starting with basic statistical moments: the mean value $m_1 = EX$ (first moment), the variance $m_2 = E(X-EX)^2$ (second moment) and its square root $S = \sqrt{E(X-EX)^2}$ (standard deviation), we are approaching the high-order moments—skewness (third moment), and kurtosis (fourth moment). The moments $m_1, \ldots, m_4$

* Corresponding author.
E-mail addresses: ssimbero@asu.cas.cz (S. Šimberová), suk@utia.cas.cz (T. Suk).

http://dx.doi.org/10.1016/j.ascom.2016.01.003
2213-1337/

were used e.g. in Leka and Barnes (2003a,b) to analyze physical parameters in active solar regions, the generalized spectral-kurtosis estimator and its statistics is in Nita and Gary (2010a,b). Aharonian et al. (2009) observed oscillations of a specific γ-ray source in the Galactic Center region. They analyzed them by the statistical moment-based Hillas technique (Hillas, 1985) based on the characteristic ellipse, i.e. second-order moments. Rimoldini (2014) proposed unbiased estimators of the weighted skewness and kurtosis moments, corrected for biases due to sample size and Gaussian noise.

The dynamic phenomena in astronomical image processing have been studied in various wavelengths. These events are often observed and described by the means of a light curve, i.e. the brightness of a specific pixel (or average brightness of some region) as a function of time. In context of moments, the light curve equals the first moment m_1. The light curves in Hα were introduced in Švestka and Simon (1969), but it was found they do not describe the event with sufficient accuracy.

Recently, Salakhutdinova and Golovko (2004) observed so called structure functions that enable deeper insight into the physical phenomena in the Sun, but do not express the fine details of the events. Nuño et al. (2008) observed fast events and magnetoacoustic waves, Jackiewicz and Balasubramaniam (2013) deal with regions both with flares and with oscillating filaments and Jardins and Canfield (2003) observed preflare phenomenon called moving blueshift events. All of them used Hα band, the last one in combination with a spectrograph and X-ray band.

Li et al. (2005) were interested in one specific event (2002 July 15) in various bands: optical continuum, Hα, UV continuum, microwave, soft X-rays and high-cadence longitudinal magnetograms. While the previous events are studied in the chromosphere, De Moortel et al. (2002a,b) observed oscillations in the corona, X-ray band. They found that loops situated above the sunspot umbras show oscillations close to 3 min, whereas non-sunspot loops (above plage regions) show oscillations close to 5 min. The flare-generated oscillations from the photosphere to the corona are described in detail in De Pontieu et al. (2005). Quasi-periodic pulsations are studied in Nakariakov and King (2007), Nakariakov and Inglis (2009), Nakariakov et al. (2010). King et al. (2003) observed quasi-periodic disturbances in extreme-ultraviolet band (171 Å and 195 Å) with two ranges of periods: 2–3 min and 5–8 min. A detailed list of relevant references can be found in Wang (2011). Data analysis has been based on the light curves in the above-mentioned cases, while our approach is based on the 3rd and higher moments.

Characteristics of the moments in the active regions during solar flares were studied in Šimberová et al. (2014) and Šimberová and Suk (2013). We found that the last two mentioned moments, skewness and kurtosis, play an important role in the study of this dynamic process. The unusual behavior of both moments was observed by chance while studying development in various areas on the solar disk in Hα images. While the first moment (the light curve) and the second moment do not provide any relevant information about the investigated area in time, the skewness and kurtosis quite clearly and unambiguously identify a "turning point" in the observed dynamical event even with the accuracy to one image plane. This turning point enables to determine the trigger area of the flare, which is important for further image analysis. Now we are able to specify the time sequence of the pre-flare phase and to study physical conditions (magnetic field distribution, density fluctuations, etc.) leading to the flare arising.

To automate the process of determining the start, it is necessary to develop a special algorithm. Searching for the trigger area leads to the turning point (i.e. the start of the increase) on a curve of skewness with respect to time. The turning point can generally be detected as maximum of second derivative. The skewness is (or could be) noisy and we do not want to detect each local maximum of the noise. Therefore, we have designed a special filter combining Gaussian smoothing with the second derivative in Šimberová et al. (2014). An automatic search for local maxima allows the division of a dynamic event into time slots, in which we want to separately perform further analysis, e.g. the time slot up to the turning point enables detailed pre-flare analysis. Of course, we can analyze the behavior of moments throughout the period of observation of the dynamic phenomenon.

In this paper we are going to study, what moment or combination of moments is optimal for image analysis. We suppose the same methodology can be applied to other dynamically developed phenomena in video sequences.

Our article is organized as follows: The next section covers the introduction of statistical high-order moments and principal components in image analysis, the 3rd section involves experiments with real datasets and frequency analysis. Summary and results are discussed in Conclusion.

2. The high-order moments and principal components in image analysis

2.1. The statistical hypermoments

The high-order moments skewness m_3 and kurtosis m_4 are in established notation

$$m_3 = E(X - EX)^3/S^3, \qquad m_4 = E(X - EX)^4/S^4, \tag{1}$$

where EX is the mean value of random variable, S is standard deviation and S^2 is variance. Continuing for $n > 4$

$$m_n = E(X - EX)^n/S^n. \tag{2}$$

The moment m_5 is sometimes called hyperskewness and m_6 hyperflatness.

On the other hand, there is also the zeroth-order moment m_0, called moment about origin. In our case it equals the area of the histogram and the area of the observed region in pixels as well.

Increasing the order of moments it describes more and more details of the histogram. Theoretically, in the case of a continuous function, we can continue up to infinity. In the case of digital image (discrete function), we have some finite L levels of brightness (typically 2^7, or 2^8, 2^9, etc.), i.e. L bins of the histogram. The moments m_0, m_1, m_2, m_3, $m_4, \ldots, m_{L-1}$ give complete description of the histogram. It also means that there are methods reconstructing the discrete function from the moments.

In practice, the finest details are just noise and the numerical precision also decreases with the moment order. Therefore it is useful to determine a maximum moment order s (much lower than L) in a specific application. We use the limit $s = 10$ in this paper, it has emerged from our experiments with reconstruction from moments— (Flusser et al., 2009), Section 6.5.

The time curves of the high-order moments are also highly correlated. This can be solved either in advance, by use of some type of orthogonal moments, or subsequently, by principal component analysis. Due to the difficulty and risk of the statistical interpretation of orthogonal moments we decided for the latter approach. The time curves of m_3, m_4, m_7 and m_{10} can be compared in Fig. 1. It can be seen that the adjacent moments are highly correlated, nonetheless, they bring new information.

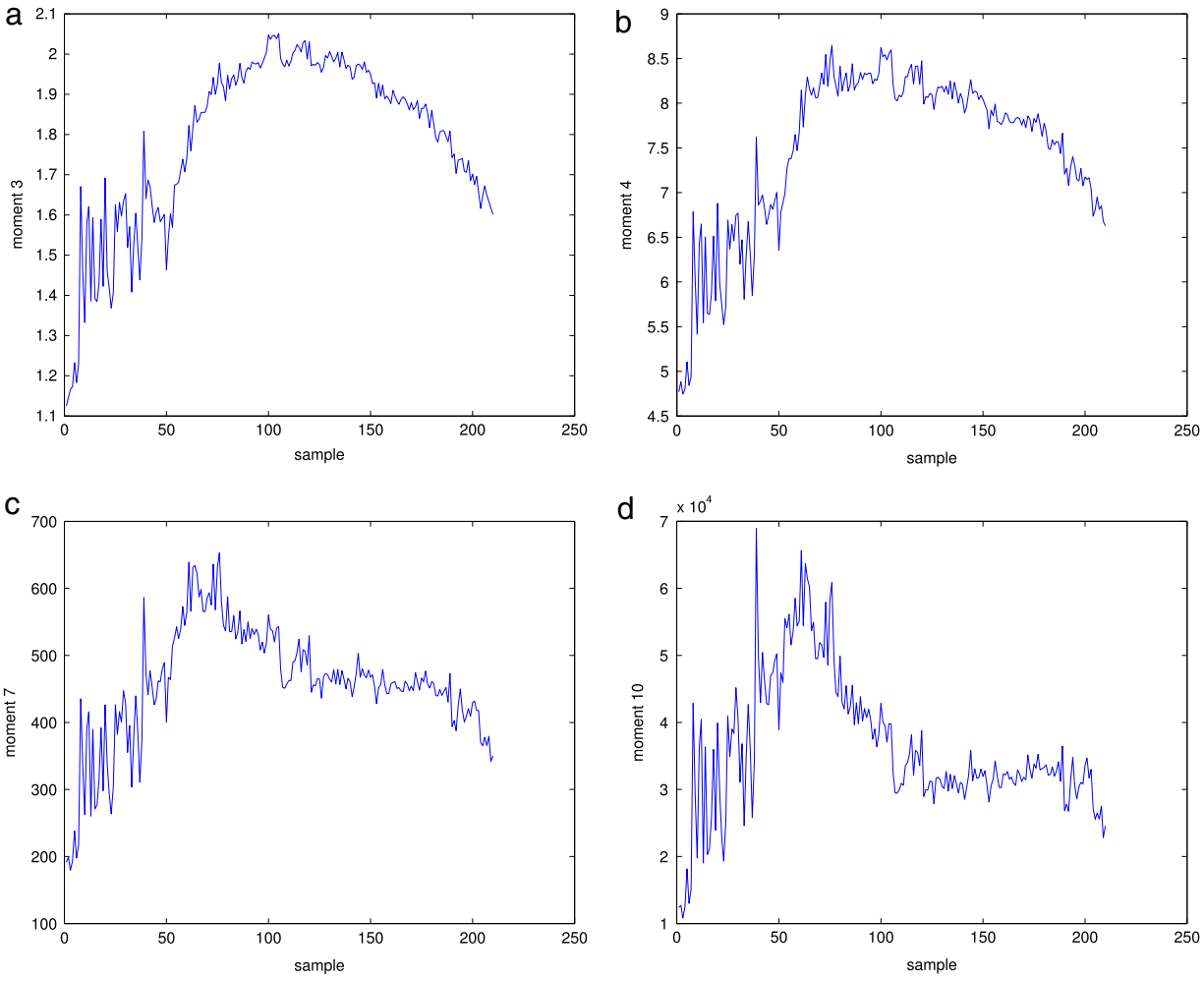

Fig. 1. Moments of the event O_031218—Ondřejov observatory. (a) m_3 (skewness), (b) m_4 (kurtosis), (c) m_7 and (d) m_{10}.

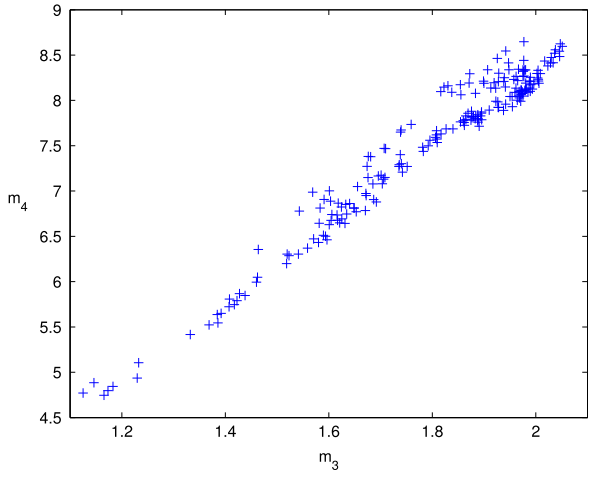

Fig. 2. Feature space of the skewness (m_3) and kurtosis (m_4).

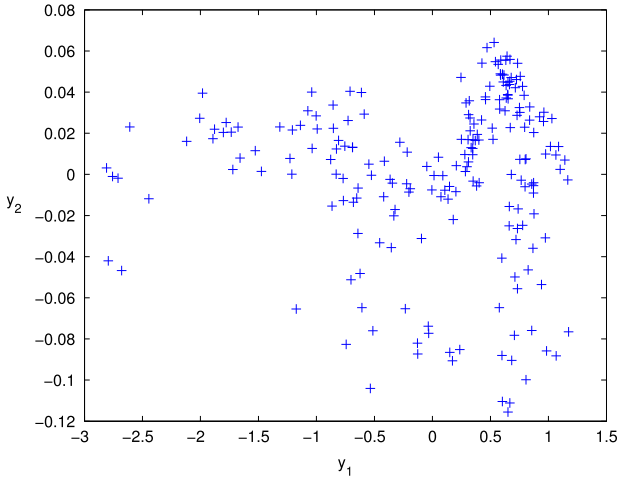

Fig. 3. Feature space of the principal components y_1 and y_2 computed from the data in Fig. 2.

2.2. Principal component analysis

Principal component analysis (PCA) is the method of data decorrelation. It belongs to the set of classic statistical methods (Murtagh and Heck, 1987). PCA is widely used in various fields of astronomy: for the analysis of spectra (e.g. Rees et al., 2000; Miller et al., 2007; Parker et al., 2014), automated classification of spectra (Bailer-Jones et al., 1998), systematic effect analysis in large datasets (Tamuz et al., 2005), detection of exoplanets (Soummer et al., 2012; Meshkat et al., 2014), etc.

Firstly, let us have two sequences of observations a_i and b_i, $i = 1, 2, \ldots, n$. We assume they are almost linearly dependent, but not completely, i.e. their correlation is high, but less than one. We would like to find out what both sequences have in common and in what ways they are different. The natural way to do it is to

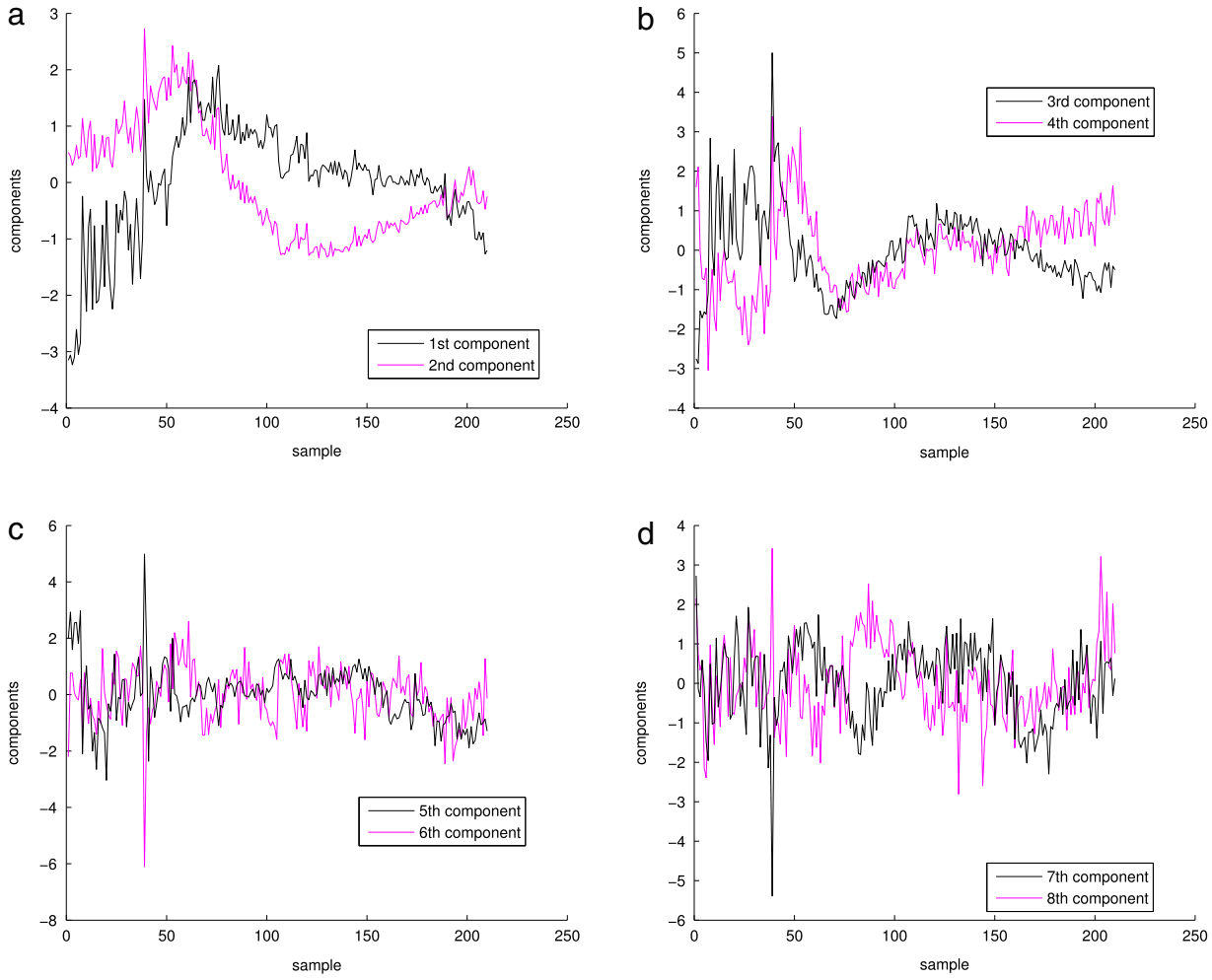

Fig. 4. Principal components of moments of orders from 3 to 8 of the event O_031218—Ondřejov observatory. (a) First and second components, (b) third and fourth components, (c) fifth and sixth components and (d) seventh and eighth components.

rotate the feature space (the values of a_i are in one axis and b_i in the other axis) so that the data should have the maximum variance in one axis and minimum in the second axis. It can be done by means of covariance matrix. First, we center the data by subtracting the time average

$$\bar{a}_i = a_i - \frac{1}{n}\sum_{i=1}^{n} a_i, \qquad \bar{b}_i = b_i - \frac{1}{n}\sum_{i=1}^{n} b_i, \tag{3}$$

consequently the covariance matrix is

$$\mathbf{C} = \begin{pmatrix} \sum_{i=1}^{n} \bar{a}_i^2 & \sum_{i=1}^{n} \bar{a}_i\bar{b}_i \\ \sum_{i=1}^{n} \bar{a}_i\bar{b}_i & \sum_{i=1}^{n} \bar{b}_i^2 \end{pmatrix}. \tag{4}$$

The eigenvectors of covariance matrix $\mathbf{C}$ define the rotation, its eigenvalues define significance of the corresponding components. More precisely, $\mathbf{C}$ is decomposed to $\mathbf{C} = \mathbf{P}\boldsymbol{\Lambda}\mathbf{P}^T$, where $\mathbf{P}$ is the matrix of the eigenvectors and $\boldsymbol{\Lambda}$ is the diagonal matrix of the eigenvalues sorted by values. When we assemble a matrix of observations

$$\mathbf{X}^T = \begin{pmatrix} \bar{a}_1 & \bar{a}_2 & \dots & \bar{a}_i & \dots & \bar{a}_n \\ \bar{b}_1 & \bar{b}_2 & \dots & \bar{b}_i & \dots & \bar{b}_n \end{pmatrix}, \tag{5}$$

then $\mathbf{C} = \mathbf{X}^T\mathbf{X}$ and the principal components can be expressed as

$$\mathbf{Y} = \mathbf{X}\mathbf{P}, \tag{6}$$

where the element y_{ij} of matrix $\mathbf{Y}$ is the jth component of the ith observation.

An example is shown in Fig. 2 with the feature space of the moments m_3 and m_4. Using the scenario of moments in Fig. 1, the eigenvalue corresponding to the first component is $\lambda_1 = 0.8594$, and the eigenvalue corresponding to the second component is $\lambda_2 = 0.0016$. Their high ratio $\lambda_1/\lambda_2 = 525$ corresponds with high correlation between them (99.972%). The feature space of the principal components is in Fig. 3. The graph in Fig. 3 has arisen from the graph in Fig. 2 by translating the centroid to the coordinate origin, rotating and strong stretching in the vertical direction. The method approximates the data in Fig. 3 by a straight line that is translated and rotated so it coincides with the x-axis.

If there are k observations ($k > 2$) in each point (or instant) i, then covariance matrix $\mathbf{C}$ has a size $k \times k$, matrices $\mathbf{P}$ and $\boldsymbol{\Lambda}$ have the same size. The method decomposes the individual vectors into the first component and the residuum projected to the subspace perpendicular to the first eigenvector of $\mathbf{C}$. Afterwards the initial residuum is decomposed to the second component and another residuum, etc., theoretically to infinity, practically until the kth component. The number of the components equals the number of input channels k.

3. Simulated data experiments

Prior to the real data applications, we tested our method on the simulated fast event. The typical time moment curve of a

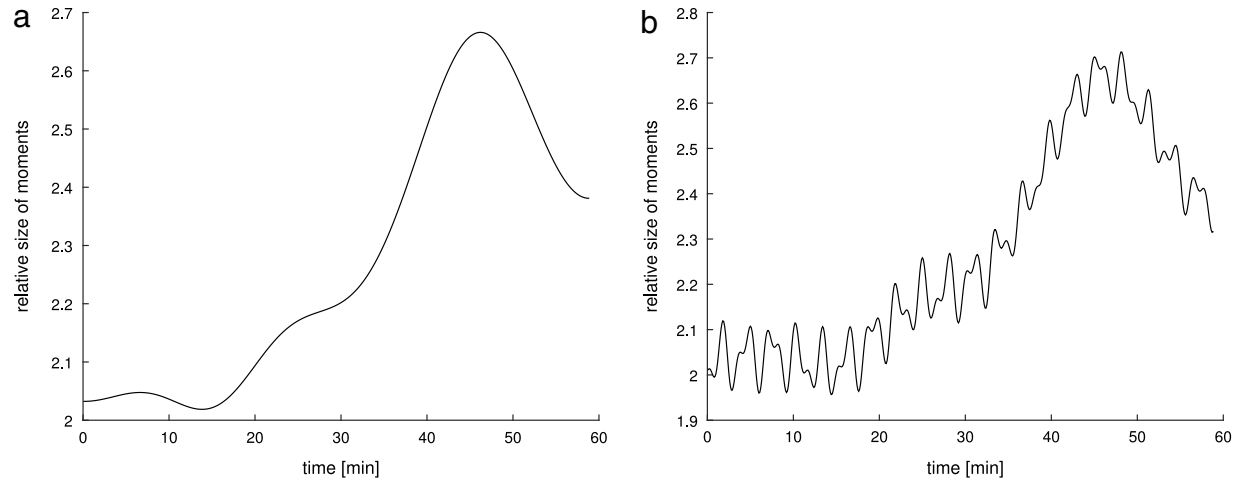

Fig. 5. Typical flare time curve used for the third moment: (a) by itself, (b) with oscillations.

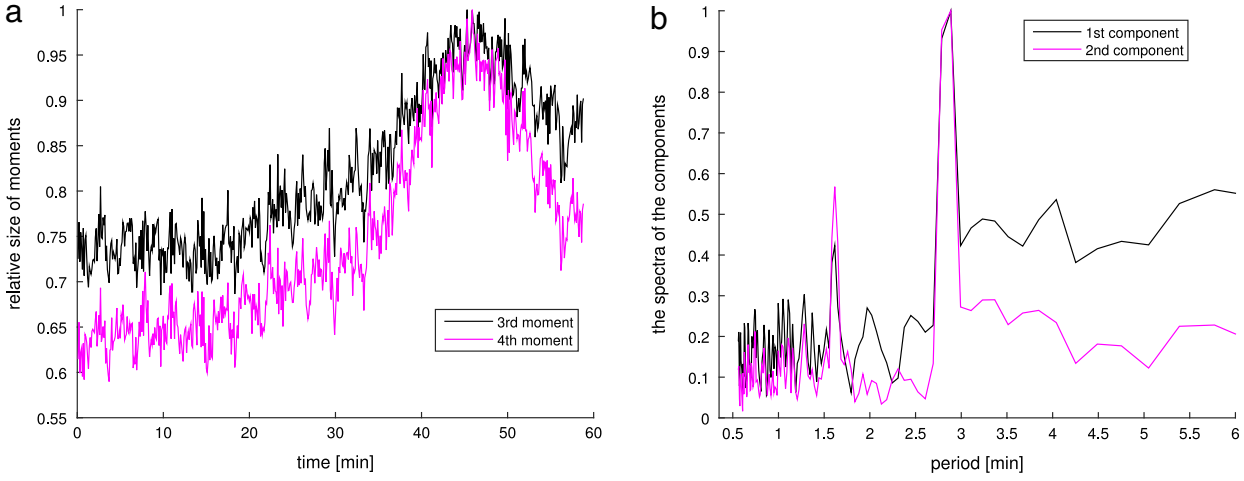

Fig. 6. Third and fourth moments with noise: (a) normalized on the unit maximum, (b) amplitude Fourier spectra of the first two principal components.

developing solar flare is in Fig. 5(a). The model curve is patterned on the real observation describing all important phases: inactive state, pre-flare, turning point, developing area with its maximum and post-flare. 588 samples with proposed distance 6 s represent the total interval 58 min. We modeled similar curves for all eight moments from m_3 to m_{10}, they differ mainly by the scaling of values. The scaling according to the maximum values of individual moment curves is: 2.67, 14.8, 82.7, 566, 4118, $3.29 \cdot 10^4$, $2.77 \cdot 10^5$ and $2.46 \cdot 10^6$ for the moments from m_3 to m_{10}, respectively. Typically, two main parts of the moment curves have been recognized: pre-flare up to the turning point (samples 1–341), and eruptive phase with its maximum (samples 342–588).

Two sinusoidal signals were added, with periods 2 min 55 s and 1 min 39 s (two typical frequencies occurring in the real data). The one with the longer period has an amplitude of 2% of the curve maximum, while the signal with the shorter period has an amplitude of 65% of the first one. These values are valid in the pre-flare phase, both curves have decreased in amplitude to 80% after the turning point. The moment time curve with the oscillations is in Fig. 5(b).

Finally, we need to take noise into consideration with the same correlation between moments in each pair as the natural signal. An appropriate solution is in Vaughan and Andersen (2003). The task is to generate a sequence of random variables $\boldsymbol{\xi} = [\xi_1, \xi_2, \ldots, \xi_n]$ with the given covariance matrix $\mathbf{C}$ and the vector of mean values $\boldsymbol{\mu}$. The Cholesky decomposition of $\mathbf{C}$ to a lower triangle form $\boldsymbol{\tau}$ so $\mathbf{C} = \boldsymbol{\tau}\boldsymbol{\tau}^T$ generating a sequence of independent random variables with Gaussian distribution $\boldsymbol{\zeta} = [\zeta_1, \zeta_2, \ldots, \zeta_n]$ with zero mean value and unit standard deviation. The result can be obtained as

$$\boldsymbol{\xi} = \boldsymbol{\tau}\boldsymbol{\zeta} + \boldsymbol{\mu}. \tag{7}$$

Our approach is slightly modified. The correlation matrix of the real data and its Cholesky decomposition is computed. Then we generated the pseudo-random variables $\boldsymbol{\zeta}$ for eight channels. Using (7) the noise $\boldsymbol{\xi}$ is determined. Finally, it is multiplied by the coefficient 2% of the corresponding moment curve maximum and added to the generated moment curves (they serve as the mean value $\boldsymbol{\mu}$ here). It means the standard deviation of the noise is the same as the amplitude of the sinusoidal signal with lower frequency, the noise is very heavy, see Fig. 6(a).

Using the simulated sequences we computed the PCA and its Fourier transformation. The eigenvalues of covariance matrix in the PCA were 7.81, $1.41 \cdot 10^{-1}$, $2.92 \cdot 10^{-2}$, $1.18 \cdot 10^{-2}$, $5.0 \cdot 10^{-3}$, $6.78 \cdot 10^{-4}$, $4.65 \cdot 10^{-4}$ and $2.19 \cdot 10^{-5}$. An example of the first two components is in Fig. 6(b). The peaks corresponding to the two added sinusoidal signals are clearly visible in all components. It means the oscillations can be detected even in heavy noise with the correct frequency.

4. Real data experiments

Besides the experiments with reconstruction of synthetic data, see Flusser et al. (2009), and our experiments with artificial

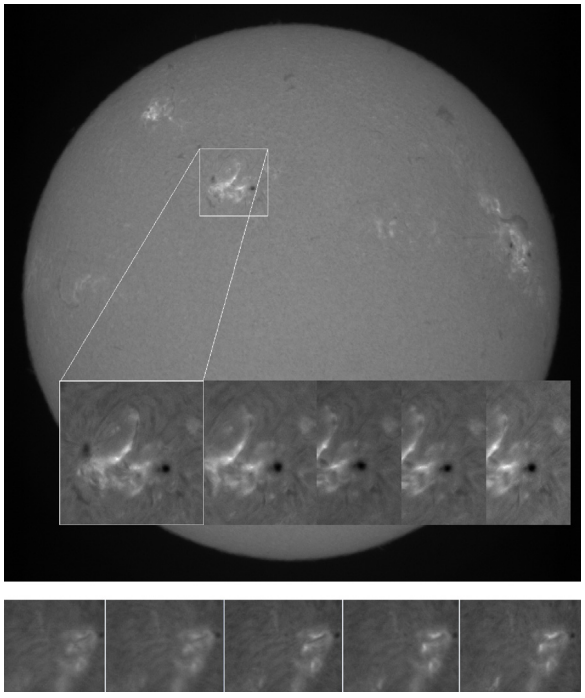

Fig. 7. Two examples of the different observed sequences: upper panel—Kanzelhöhe observatory, bottom panel—Ondřejov observatory.

sequences, we applied our method to the time sequences from real ground-based observations. There were six various events used from two different solar telescopes observed in Hα line. Two kinds of files differ in the size of their angular resolution, the full-disk observation— Kanzelhöhe with resolution 1 pix $=$ 1.02 $\times$ 1.02 arcsec (two events) and detail observation—Ondřejov with resolution 1 pix $=$ 0.5 $\times$ 0.5 arcsec (four events), see Fig. 7. Traditional digitization to 256 gray levels was applied. Examples of the image datasets can be found on the web pages (Astronomical Institute ASCR, 2014) and in Kanzelhöhe Observatory for Solar and Environmental Research (2014).

The signal sampling is given by observational mode. It depends on the phase of a dynamic event. We interpolated the signal according to the highest sampling frequency, i.e. Ondřejov data 12 images/min, Kanzelhöhe data 10 images/min.

4.1. Principal component analysis

As an example the method has been applied to high resolution data (event O_031218—Ondřejov observatory). The mutual dependence of the data can be seen in Figs. 2 and 3. It is a proof of correlation between moments m_3 and m_4. The eight moments from m_3 to m_{10} have been used in this experiment. Their dynamic range dramatically increases, m_3 has values from 1.13 to 2.05 while m_{10} from $1.08 \cdot 10^4$ to $6.89 \cdot 10^5$. It is a good reason to normalize the moments by their standard deviations (known as a z-score)

$$\bar{m}_i(t) = m_i(t) / \left[\frac{1}{n-1} \sum_{t=t_0}^{t_n} \left(m_i(t) - \frac{1}{n} \sum_{t=t_0}^{t_n} m_i(t) \right)^2 \right]. \qquad (8)$$

Then PCA follows. The eigenvalues are 6.70, 1.28, $1.69 \cdot 10^{-2}$, $8.40 \cdot 10^{-4}$, $5.29 \cdot 10^{-5}$, $7.35 \cdot 10^{-7}$, $6.43 \cdot 10^{-8}$ and $1.47 \cdot 10^{-9}$. The first component is an approximate average of the moments. It can be understood as a typical shape of the moment curve, it shows what is common for all the moments. The higher components involve both positive and negative coefficients. The second component shows a difference between very high-order moments from m_7 to m_{10} and lower-order ones from m_3 to m_6. The higher components also represent differences among the moments.

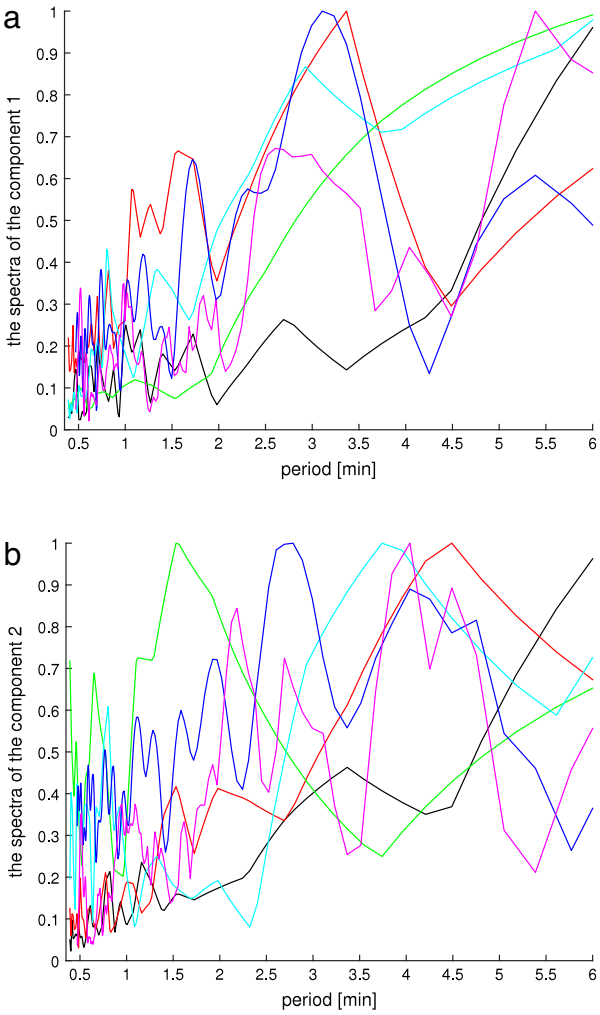

Fig. 8. Fourier spectrum of (a) the first component, (b) the second component. The spectrum is non-traditionally expressed against period, not against frequency. Legend: — O_031218 (black), — O_030319 (red), — O_030221 (green), — O_030212 (cyan), — K_110910 (blue) and — K_110307 (magenta).

The result – individual components – is in Fig. 4. To be able to compare them, we have divided the components by the square root of the corresponding eigenvalue.

4.2. Frequency analysis

To contribute to the flare diagnostics we are interested in the occurrence of certain oscillations in a sequence of active region images. A good summary of their observations in various wavelengths is in Wang (2011), analysis in Hα is also in Šimberová and Suk (2013).

The pre-flare phase of our sample case can be seen in Fig. 1 at the beginning of the moment curves (samples from 8 to 53). The basic mean of the frequency analysis is a Fourier transformation. The amplitude spectrum of the first principal component from all six investigated events is shown in Fig. 8(a).

The horizontal axis of the Fourier spectrum contains periods in minutes instead of frequency. Then we can compare the periods of the oscillations directly with the results published in other articles. There were both two-minute oscillations (period between 1.5 and

Table 1
Lengths and periods of the two most relevant maxima of the Fourier spectra of the first principal components.

Event	O_031218	O_030319	O_030221	O_030212	K_110910	K_110307
Length	17 min 30 s	17 min 30 s	10 min 0 s	15 min 0 s	80 min 48 s	58 min 48 s
1st max.	2 min 42 s	3 min 22 s	1 min 6 s	2 min 56 s	3 min 0 s	2 min 36 s
2nd max.	1 min 44 s	1 min 34 s	–	1 min 21 s	1 min 45 s	1 min 50s

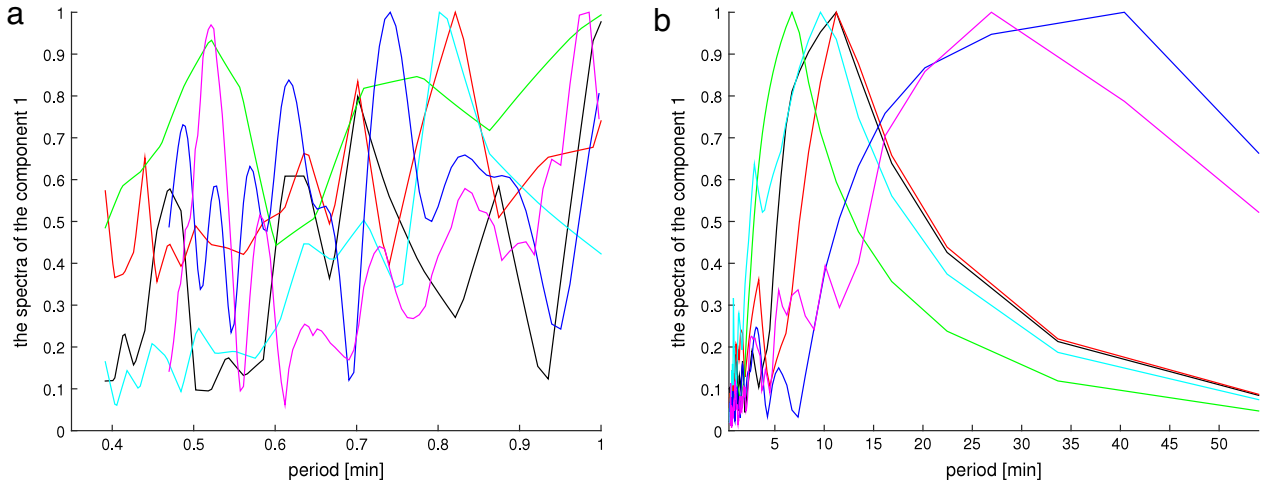

Fig. 9. Fourier spectrum of the first component—(a) detail of periods less than 1 minute, (b) whole spectrum including all maxima. Legend: — O_031218 (black), — O_030319 (red), — O_030221 (green), — O_030212 (cyan), — K_110910 (blue) and — K_110307 (magenta).

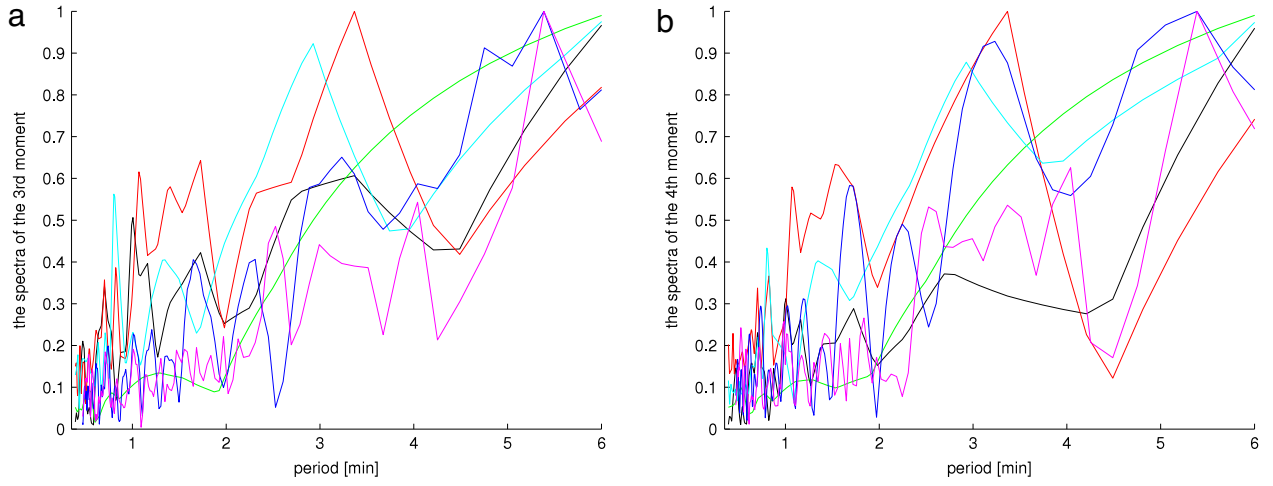

Fig. 10. Fourier spectrum of (a) the third-order moment, (b) the fourth-order moment. Legend: — O_031218 (black), — O_030319 (red), — O_030221 (green), — O_030212 (cyan), — K_110910 (blue) and — K_110307 (magenta).

2 min) and three-minute oscillations (period between 2 min 36 s and 3 min 22 s) in five events: O_031218, O_030319, O_030212, K_110910 and K_110307. The event O_030221 is not so typical, it has only one maximum at 1 min 6 s. The events K_110910 and K_110307 have additional maxima at 5 min 23 s. The maxima of K_110307 are peculiarly double, there is a weaker maximum at 3 min 0 s beside 2 min 36 s and another weaker maximum at 1 min 58 s beside 1 min 50 s.

The results of all processed events are summarized in Table 1. The three-minute and five-minute oscillations are in correspondence with the results of De Moortel et al. (2002a,b), Wang (2011) and King et al. (2003).

Other maxima are not so relevant—the shorter periods represent noise (see Fig. 9(a)) and the longer ones express the whole length of the event (see Fig. 9(b)).

Comparison with the spectrum of the second principal component is in Fig. 8(b). While the two-minute oscillations are roughly similar, the three-minute maxima were shifted to four minutes (excluding O_031218). Nevertheless, if the oscillations are only visible in the second component, it means they are only visible in some moment curves. This is because they are not as important as those of the first component.

Comparison with the spectrum of the third moment is in Fig. 10(a) and with the spectrum of the fourth moment in Fig. 10(b). The main difference from Fig. 8(a) is in the significance of some maxima, particularly the event O_031218 has two significant maxima at 1 min 44 s and at 3 min 20 s in the third moment spectrum and also high value at 2 min 42 s. The last value is not local maximum here, but it is the local maximum detected in all higher moments. The value corresponding to 3 min 20 s is low in all higher moments. Therefore PCA evaluated the maximum at 2 min 42 s as significant and that at 3 min 20 s as non-significant.

Additional less significant maxima can be seen in the spectra of the third and fourth components in Fig. 11(a) and (b).

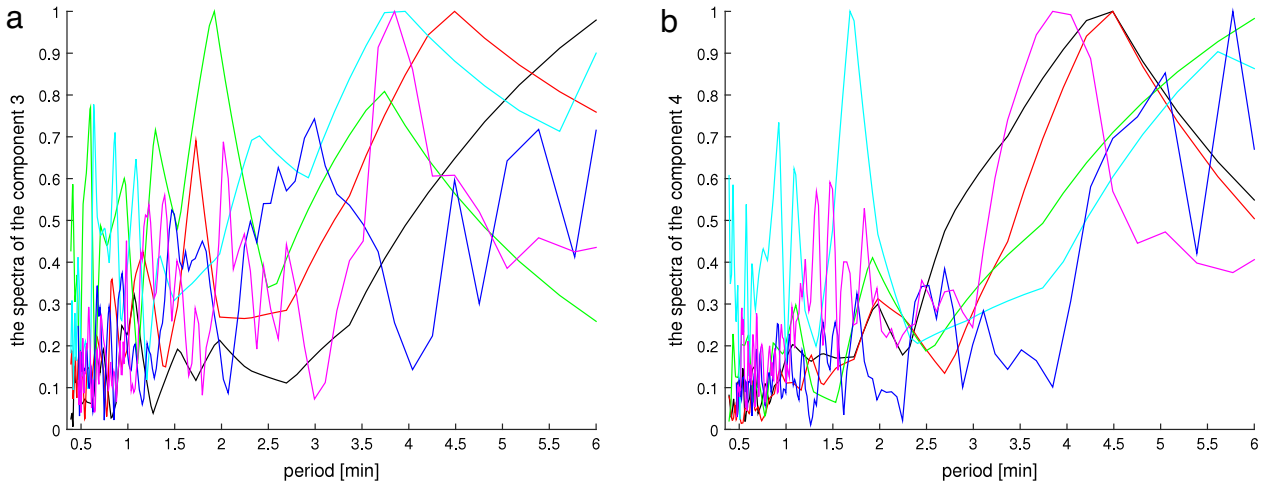

Fig. 11. Fourier spectrum of (a) the third component, (b) the fourth component. Legend: — O_031218 (black), — O_030319 (red), — O_030221 (green), — O_030212 (cyan), — K_110910 (blue) and — K_110307 (magenta).

5. Conclusions

The statistical moments of high orders (HOMs) express the form of a dynamic process. We developed methodology for the use of HOMs computed from histograms in a video–image analysis and we performed experiments with the real data video sequences—solar flares observed in a Hα line. Development of a dynamic phenomenon causes the changes in the histogram of individual frames in a video sequence and the HOMs provide valuable information about these changes.

The HOMs are highly correlated and it raises the question of how many orders of moments are sufficient for the description and analysis of the process. We proposed the PCA method for the frequency analysis of the investigated event; it yields both the decorrelated components for additional analysis and eigenvalues of the covariance matrix for judgment of their significance. In the decomposition of the signal to an ith component and a residuum, the significance of the residuum depends on their correlation: the higher the correlation, the less significant the residuum. To the best of our knowledge the combination of these kind of moments with PCA has not yet been used in this way.

The HOMs describe a dynamic process more precisely than older methods using light curve analysis. Our method based inventively on HOMs is not sensitive to angular resolution of the video sequence, it can work both with a specified area of the whole solar disk and with high resolution detail. Our approach is also robust to noise—the moment represents an integral functional over the region of interest, then the noise is removed by averaging over this area. The robustness to noise was tested on simulated data. This method can also work with a high range of sampling frequencies. When the observational mode has been set to a lower frequency of sampling, gaps can be filled by interpolation. The undersampling often occurs when the active regions are just searched and it is not clear whether the flare occurs at all. The real data experiments have shown that interpolation does not violate the lower frequencies.

The frequency analysis of the components by Fourier transformation can give information about various oscillations and quasi-oscillations in the process. There are two limits in the frequency analysis: the sampling frequency limits the minimal periods of the analyzed oscillations, and the length of the sequence limits the maximal periods. The optimal order of the moments strongly depends on the dynamics of the phenomenon and on other properties of recorded video sequence. Our experiments have shown it is sufficient to compute the moments from the third to about the eighth order and then to use the first two components (three components at maximum) from PCA in the case of solar flare events. These numbers can differ in the case of other processes. This methodology is suitable not only for solar flare analysis, but also for the investigation of other dynamic processes.

Acknowledgments

This research was supported by Czech Science Foundation (GAČR) Grant No. GA15-16928S and The Czech Academy of Sciences (AV ČR) Grant No. RVO:67985815.

Thanks to Astrid Veronig and Wolfgang Hirtenfellner-Polanec (Uni-Graz and Observatory Kanzelhöhe), and František Zloch (Observatory Ondřejov) for their help in accessing image databases and event hunting.

References

Aharonian, F., Akhperjanian, A., Anton, G., de Almeida, U.B., Bazer-Bachi, A., Becherini, Y., Behera, B., Bernlöhr, K., Boisson, C., Bochow, A., Borrel, V., Braun, I., Brion, E., Brucker, J., Brun7, P., Bühler, R., Bulik, T., Büsching, I., Boutelier, T., Chadwick, P., Charbonnier, A., Chaves, R., Cheesebrough, A., Chounet, L.-M., Clapson, A., Coignet, G., Dalton, M., Daniel, M., Davids, I., Degrange, B., Deil, C., Dickinson, H., Djannati-Ataï, A., Domainko, W., Drury, L., Dubois, F., Dubus, G., Dyks, J., Dyrda, M., Egberts, K., Emmanoulopoulos, D., Espigat, P., Farnier, C., Feinstein, F., Fiasson, A., Förster, A., Fontaine, G., Füßling, M., Gabici, S., Gallant, Y., Gérard, L., Giebels, B., Glicenstein, J., Glück, B., Goret, P., Hauser, D., Hauser, M., Heinz, S., Heinzelmann, G., Henri, G., Hermann, G., Hinton, J., Hoffmann, A., Hofmann, W., Holleran, M., Hoppe, S., Horns, D., Jacholkowska, A., de Jager, O., Jung, I., Katarzyński, K., Katz, U., Kaufmann, S., Kendziorra, E., Kerschhaggl, M., Khangulyan, D., Khélifi, B., Keogh, D., Komin, N., Kosack, K., Lamanna, G., Lenain, J.-P., Lohse, T., Marandon, V., Martin6, J., Martineau-Huynh, O., Marcowith, A., Maurin, D., McComb, T., Medina, M., Moderski, R., Moulin, E., Naumann-Godo, M., de Naurois, M., Nedbal, D., Nekrassov, D., Niemiec, J., Nolan, S., Ohm, S., Olive, J.-F., de Oña Wilhelmi, E., Orford, K., Ostrowski, M., Panter, M., Arribas, M.P., Pedaletti, G., Pelletier, G., Petrucci, P.-O., Pita, S., Pühlhofer, G., Punch, M., Quirrenbach, A., Raubenheimer, B., Raue, M., Rayner, S., Renaud, M., Rieger, F., Ripken, J., Rob, L., Rolland, L., Rosier-Lees, S., Rowell, G., Rudak, B., Rulten, C., Ruppel, J., Sahakian, V., Santangelo, A., Schlickeiser, R., Schöck, F., Schröder, R., Schwanke, U., Schwarzburg, S., Schwemmer, S., Shalchi, A., Skilton, J., Sol, H., Spangler, D., Stawarz, L., Steenkamp, R., Stegmann, C., Superina, G., Szostek, A., Tam, P., Tavernet, J.-P., Terrier, R., Tibolla, O., van Eldik, C., Vasileiadis, G., Venter, C., Venter, L., Vialle, J., Vincent, P., Vivier, M., Völk, H., Volpe, F., Wagner, S., Ward, M., Zdziarski, A., Zech, A., 2009. Spectrum and variability of the galactic center vhe γ-ray source hess j1745-290. Astron. Astrophys. 503, 817–825. doi:10.1051/0004-6361/200811569.

Astronomical Institute ASCR, 2014. Data archives. http://www.asu.cas.cz/en/research/data-archives.

Bailer-Jones, C.A.L., Irwin, M., von Hippel, T., 1998. Automated classification of stellar spectra—II. Two-dimensional classification with neural networks and principal components analysis. Mon. Not. R. Astron. Soc. 298, 361–377. doi:10.1046/j.1365-8711.1998.01596.x.

De Moortel, I., Hood, A.W., Ireland, J., Walsh, R.W., 2002a. Longitudinal intensity oscillations in coronal loops observed with TRACE. Sol. Phys. 209 (1), 89–108. doi:10.1023/A:1020960505133.

De Moortel, I., Ireland, J., Walsh, R.W., Hood, A.W., 2002b. Longitudinal intensity oscillations in coronal loops observed with TRACE. Sol. Phys. 209 (1), 61–88. doi:10.1023/A:1020956421063.

De Pontieu, B., Erdélyi, R., De Moortel, I., 2005. How to channel photospheric oscillations into the corona. Astrophys. J. 624 (1), L61–L64. doi:10.1086/430345.

Dudewicz, E.J., Mishra, S., 1988. Modern Mathematical Statistics. Wiley, New York.

Flusser, J., Suk, T., Zitová, B., 2009. Moments and Moment Invariants in Pattern Recognition. Wiley, Chichester, doi:10.1002/9780470684757.

Hillas, A.M., 1985. Cerenkov light images of eas produced by primary gamma. In: 19th International Cosmic Ray Conference ICRC'85, vol. 3. NASA, pp. 445–448.

Jackiewicz, J., Balasubramaniam, K.S., 2013. Solar h-α oscillations from intensity and Doppler observations. Astrophys. J. 765, 15. doi:10.1088/0004-637X/765/1/15.

Jardins, A.C.D., Canfield, R.C., 2003. Preflare phenomena in eruptive flares. Astrophys. J. 598 (1), 678–682. doi:10.1086/378673.

Kanzelhöhe Observatory for Solar and Environmental Research, 2014. Gallery. http://www.kso.ac.at/downloads/sonnenaufnahmen_en.php.

King, D.B., Nakariakov, V.M., Deluca, E.E., Golub, L., McClements, K.G., 2003. Propagating euv disturbances in the solar corona: Two-wavelength observations. Astron. Astrophys. 404, L1–L4. doi:10.1051/0004-6361:20030763.

Leka, K.D., Barnes, G., 2003a. Photospheric magnetic field properties of flaring versus flare-quiet active regions. I. Data, general approach, and sample results. Astron. J. 595, 1277–1295. doi:10.1086/377511.

Leka, K.D., Barnes, G., 2003b. Photospheric magnetic field properties of flaring versus flare-quiet active regions. II. Discriminant analysis. Astron. J. 595, 1296–1306. doi:10.1086/377512.

Li, J., Mickey, D.L., LaBonte, B.J., 2005. The X3 flare of 2002 July 15. Astrophys. J. 620 (2), 1092–1100. doi:10.1086/427205.

Meshkat, T., Kenworthy, M.A., Quanz, S.P., Amara, A., 2014. Optimized principal component analysis on coronagraphic images of the fomalhaut system. Astrophys. J. 780, 17. arXiv:1310.8577 doi:10.1088/0004-637X/780/1/17.

Miller, L., Turner, T.J., Reeves, J.N., George, I.M., Kraemer, S.B., Wingert, B., 2007. The variable X-ray spectrum of Markarian 766. I. Principal components analysis. Astron. Astrophys. 463, 131–143. doi:10.1051/0004-6361:20066548.

Murtagh, F., Heck, A., 1987. Multivariate Data Analysis. Reidel, Dordrecht.

Nakariakov, V.M., Inglis, A.R., 2009. A multi-periodic oscillatory event in a solar flare. Astron. Astrophys. 493, 259–266. doi:10.1051/0004-6361:200810473.

Nakariakov, V.M., Inglis, A.R., Zimovets, I.V., Foullon, C., Verwichte, E., Sych, R., Myagkova, I.N., 2010. Oscillatory processes in solar flares. Plasma Phys. Control. Fusion 52, 7. doi:10.1088/0741-3335/52/12/124009.

Nakariakov, V.M., King, D.B., 2007. Coronal periodmaps. Sol. Phys. 241, 397–409. doi:10.1007/s11207-007-0348-x.

Nita, G.M., Gary, D.E., 2010a. Statistics of the spectral kurtosis estimator. Publ. Astron. Soc. 122, 595–607. doi:10.1086/652409.

Nita, G.M., Gary, D.E., 2010b. The generalized spectral kurtosis estimator. Mon. Not. R. Astron. Soc. 406, L60–L64. doi:10.1111/j.1745-3933.2010.00882.x.

Nuño, B.S.-A., González, N.B., Rodríguez, J.B., Kneer, F., Puschmann, K.G., 2008. Fast events and waves in an active region of the sun observed in hα with high spatial resolution. Astron. Astrophys. 486, 577–587. doi:10.1051/0004-6361:20079231.

Parker, M.L., Marinucci, A., Brenneman, L., Fabian, A.C., Kara, E., Matt, G., Walton, D.J., 2014. Principal component analysis of MCG-06-30-15 with XMM-Newton. Mon. Not. R. Astron. Soc. 437, 721–729. arXiv:1310.1945 doi:10.1093/mnras/stt1925. [astro-ph.HE].

Rees, D.E., López Ariste, A., Thatcher, J., Semel, M., 2000. Fast inversion of spectral lines using principal component analysis. I. Fundamentals. Astron. Astrophys. 355, 759–768.

Rimoldini, L., 2014. Weighted skewness and kurtosis unbiased by sample size and Gaussian uncertainties. Astron. Comput. 5, 1–8. doi:10.1016/j.ascom.2014.02.001.

Salakhutdinova, Irina, I., Golovko, Aleksey, A., 2004. The variations of the scaling parameters of the structure functions in solar active regions at the pre-flare stage. Sol. Phys. 225 (1), 59–74. doi:10.1007/s11207-004-2720-4.

Šimberová, S., Karlický, M., Suk, T., 2014. Statistical moments of active-region images during solar flares. Sol. Phys. 289 (1), 193–209. doi:10.1007/s11207-013-0334-4.

Šimberová, S., Suk, T., 2013. Analysis of dynamic processes by statistical moments of high orders. In: Progress in Pattern Recognition, Image Analysis, Computer Vision, and Applications, Proceedings of the 18th Iberoamerican Congress, CIARP'13, Part I. In: Lecture Notes in Computer Science, vol. 8258. Springer, pp. 221–228.

Soummer, R., Pueyo, L., Larkin, J., 2012. Detection and characterization of exoplanets and disks using projections on Karhunen-Loève eigenimages. Astrophys. J. Lett. 755, L28. arXiv:1207.4197 doi:10.1088/2041-8205/755/2/L28.

Švestka, Z., Simon, P., 1969. Proton flare project, 1966. Sol. Phys. 10 (1), 3–59. doi:10.1007/BF00146153.

Tamuz, O., Mazeh, T., Zucker, S., 2005. Correcting systematic effects in a large set of photometric light curves. Mon. Not. R. Astron. Soc. 356, 1466–1470. doi:10.1111/j.1365-2966.2004.08585.x.

Vaughan, R., Andersen, J.B., 2003. Channels, Propagation and Antennas for Mobile Communications. In: IET Electromagnetic Waves Series, vol. 50. Institution of Electrical Engineers, doi:10.1049/PBEW050E.

Wang, T., 2011. Standing slow-modewaves in hot coronal loops: Observations, modeling, and coronal seismology. Space Sci. Rev. 158 (2–4), 397–419. doi:10.1007/s11214-010-9716-1.